Journal of Advanced Ceramics
先进陶瓷
ISSN 2226-4108
CN 10-1154/TQ
清華大学出版社 Tsinghua University Press
SciOpen

*J Adv Ceram* 2026, **15**: 9221416

https://doi.org/10.26599/JAC.2026.9221416

Research Article

Just Accepted

# $Ag_2Te$ interfacial diffusion and phase transition induced built-in electric field evolution for synergistically enhanced thermoelectric performance of $Bi_2Te_{2.5}Se_{0.5}$

Shifang Ma [1,*], Daming Du [1], Ming Lin [1], Qi Luo [1], Jinzhao Guan [1], Shaoqiu Ke [3], Cuncheng Li [4], Jian Yu [1,*], Zhiyuan Liu [2,*]

[1] *Jiangxi provincial Key Laboratory of Surface Engineering, School of Materials Science and Engineering, Jiujiang University, Jiujiang 332005, China*

[2] *Advanced Ceramics Research Center, School of Materials Science and Engineering, Anhui University of Technology, Maanshan 243002, China*

[3] *State Key Laboratory of Advanced Technology for Materials Synthesis and Processing, Wuhan University of Technology, Wuhan 430070, China.*

[4] *School of Materials Science and Engineering, Shandong University of Technology, Zibo 255000, China*

[*] Corresponding authors.

E-mail: S. Ma, shifangma@163.com;

J. Yu, jianyujju@126.com;

Y. Liu, zhiyuanliu826@ahut.edu.cn

Received: September 20, 2026; Revised: November 9, 2026; Accepted: November 24, 2026

©The Author(s) 2026

Just Accepted

**Abstract:** N-type $Bi_2Te_{2.5}Se_{0.5}$ alloys exhibit a severe donor-like effect during powder metallurgy fabrication, which gives rise to excessively carrier concentration and degraded near-room-temperature thermoelectric performance. Suppressing the donor-like effect while preserving high carrier mobility remains a major bottleneck. Herein, $Ag_2Te/Bi_2Te_{2.5}Se_{0.5}$ composites are fabricated via mechanical alloying and spark plasma sintering. Owing to interfacial diffusion between superionic $Ag_2Te$ and the $Bi_2Te_{2.5}Se_{0.5}$ matrix, some Ag atoms occupy dual crystallographic sites by substituting at Bi lattice sites and intercalating into van der Waals gaps, which suppresses the donor-like effect and lowers the carrier concentration. At the phase-transition point of $Ag_2Te$ at ~420 K, reversal of the built-in electric field at the heterogeneous-interface enables enhanced carrier mobility below the transition temperature. Total thermal conductivity reduction originates from both decreased carrier thermal conductivity and suppressed lattice thermal conductivity induced by multiscale defects. The AT04 composite delivers a peak *ZT* of 1.23 at 410 K. At room temperature, the *ZT* of AT04 is 0.98, corresponding to an 80% enhancement relative to pristine $Bi_2Te_{2.5}Se_{0.5}$ (*ZT* = 0.54). This work provides new mechanistic insights and an effective strategy for utilizing phase-transition-tunable hetero-interfaces to boost the thermoelectric performance of $Bi_2Te_3$ and other thermoelectric materials.

**Keywords:** thermoelectric materials; interfacial diffusion reaction; donor-like effect; built-in electric field

## 1. Introduction

Thermoelectric (TE) materials, which enable direct conversion between thermal and electrical energy, underpin a simple, eco-friendly solid-state technology [1-3]. Operating without moving parts or refrigerants and featuring fast response times, TE devices are well suited for power generation, refrigeration, and thermal management applications [4-6]. The TE performance is determined by the dimensionless figure of merit, $ZT=\alpha^2\sigma T/(\kappa_E+\kappa_L)$ [7-9]. In this formula, $\alpha$ denotes the Seebeck coefficient, $\sigma$ is electrical conductivity, $T$ denotes absolute temperature, and $\kappa_E$ and $\kappa_L$ stand for the carrier thermal conductivity and lattice thermal conductivity, respectively. $\kappa_L$ is associated with phonon transport, whereas other key TE parameters are strongly coupled to carrier transport, giving rise to complex interdependencies [10,11]. Therefore, reducing $\kappa_L$ and achieving synergistic optimization of carrier-related parameters constitute the primary strategies for enhancing TE properties.

Among many TE material systems, $Bi_2Te_3$-based alloys are still the dominant commercial material systems for power generation, refrigeration, and thermal management applications. To date, carrier engineering and phonon engineering have become the two primary approaches for regulating the carrier and phonon transport. Carrier engineering primarily modulates carrier concentration via doping with CuI [12], $WCl_6$ [13], Ag [14] and Na [15] doping, thereby optimizing carrier-related parameters and improving the TE performance of materials. Phonon engineering reduces $\kappa_L$ by grain refinement or introducing nanophases. Techniques such as melt-spinning [16,17], ball-milling [18-20] and solvothermal synthesis [21,22] can refine grains and introduce abundant grain boundaries, thereby strengthening phonon scattering and significantly improving TE properties. Nanocompositing introduces nanoscale secondary phases, such as metal-organic framework (MOF) [23], SiC [24], $TiO_2$ [25] and B [26], into the matrix to strengthen phonon scattering at heterogeneous interfaces and lower $\kappa_L$. While phonon engineering has been successfully implemented to improve the TE performance of *p*-type $Bi_2Te_3$-based alloys, comparable $ZT$

Just Accepted

improvements have not been realized for their *n*-type counterparts.

For $Bi_2Te_3$-based alloys, the significant property disparity between *p*-type and *n*-type counterparts hinders the development of high-performance TE devices. The inferior performance of *n*-type $Bi_2Te_3$-based alloys mainly originates from the donor-like effect that arises during material preparation and sintering. The donor-like effect originates from Te-vacancy-related point defects generated during powder metallurgy processing. These defects serve as electron donors and yield excessively high carrier concentration. Meanwhile, grain boundaries and structural defects simultaneously scatter charge carriers, thus degrading carrier mobility. A major challenge for *n*-type $Bi_2Te_3$-based alloys lies in simultaneously suppressing the donor-like effects and optimizing carrier mobility. In recent research, an alternative strategy is the introduction of metastable alloys ($AgBiSe_2$ [27], $MnSb_2Se_4$ [28] and $Cu_8GeSe_6$ [29]) into $Bi_2Te_3$ materials. The interfacial diffusion reactions induced by these alloys are utilized to regulate the carrier concentration, thereby counteracting the excessive carrier concentration caused by donor-like effects. Nevertheless, these strategies often cannot preserve high carrier mobility and may even inadvertently increase carrier concentration, leaving the underlying donor-like effect unresolved. Although they can suppress the donor-like effect to a certain degree, they fail to achieve concurrent improvements in carrier mobility. Therefore, future strategies should be designed to simultaneously mitigate donor-like behavior and improve carrier mobility to realize synergistic enhancement of carrier-related transport for high-performance room-temperature TE applications. Although introducing $Ag_2Te$ has been reported to improve the TE performance of *n*-type $Bi_2Te_{2.7}Se_{0.3}$ composites [30], atomic-scale evidence for Ag dual-site occupation remains ambiguous. Furthermore, the temperature-dependent evolution of carrier mobility driven by the $Ag_2Te$ phase-transition-modulated interfacial electronic structure has seldom been investigated.

Herein, to suppress donor-like effects and optimize carrier-related transport performance, *n*-type

Just Accepted

$Bi_2Te_{2.5}Se_{0.5}$ composites incorporated with superionic $Ag_2Te$ were designed and fabricated. The rationale for selecting $Ag_2Te$ as the second phase is as follows: (i) $Ag_2Te$ is a superionic conductor with a phase transition at 420 K, enabling a tunable interfacial electronic structure near room temperature; (ii) it exhibits favorable intrinsic TE properties and does not significantly deteriorate the performance of the matrix; (iii), Ag can diffuse into the $Bi_2Te_{2.5}Se_{0.5}$ lattice during spark plasma sintering, enabling dual-site occupation and suppression of the donor-like effect; and (iv) the $Ag_2Te/Bi_2Te_{2.5}Se_{0.5}$ heterointerface can modulate carrier transport via band alignment. These characteristics differentiate $Ag_2Te$ from conventional inert second phases, rendering it suitable for tuning the TE performance of $Bi_2Te_{2.5}Se_{0.5}$. More importantly, the direction of built-in electric field at the heterogeneous interface reverses at the $Ag_2Te$ phase-transition temperature. This phenomenon explains the anomalous temperature dependence of carrier mobility. Accordingly, interfacial diffusion reactions triggered by incorporating superionic $Ag_2Te$ during spark plasma sintering can optimize carrier-related parameters, increase the power factor, and reduce the thermal conductivity, thereby synergistically regulating electron and phonon transport. This work provides new mechanistic insights and an effective strategy for utilizing phase-transition-tunable hetero-interfaces to enhance $Bi_2Te_3$ and other TE materials.

## 2. Experimental

In this work, elemental powders of Bi (99.999%), Te (99.999%), Se (99.999%) and Ag (99.99%) were employed as starting raw materials. Powders were weighed according to the nominal stoichiometries of $Bi_2Te_{2.5}Se_{0.5}$ and $Ag_2Te$. $Bi_2Te_{2.5}Se_{0.5}$ and $Ag_2Te$ powders were separately synthesized via mechanically alloying in a planetary ball milling for 8 h. The obtained alloy powders were hand-mixed to prepare $x$ wt% $Ag_2Te/Bi_2Te_{2.5}Se_{0.5}$ composite powders ($x$ = 0, 0.2, 0.4, 0.6, 0.8), where $x$ represents the nominal mass fraction of $Ag_2Te$ in the composite. Bulk materials were fabricated by spark plasma sintering (SPS) at 723 K for 5 min under an applied pressure of 50 MPa.

Just Accepted

Crystal structures of all specimens were characterized using an X-ray diffractometer (XRD, Rigaku SmartLab) with Cu $K\alpha$ radiation over the 2θ range from 10° to 80°. Electron probe microanalysis (EPMA) (JEOL, JXA-8230) equipped with wavelength dispersive spectroscopy (WDS) was utilized to examine chemical composition and elemental distribution. Microstructures, atomic structures, and elemental distribution of the $Ag_2Te/Bi_2Te_{2.5}Se_{0.5}$ composites were characterized via scanning transmission electron microscopy combined with high angle annular dark-field (STEM-HAADF) and scanning transmission electron microscopy coupled with energy dispersion X-ray spectroscopy (STEM-EDX) techniques. STEM lamellae were prepared using a focused ion beam (FIB) system (Helios Nanolab G3 UC, FEI). Sintered bulk sample were cut into rectangular specimens with approximate dimensions of 2.5×3.5×12 mm. Due to the intrinsic anisotropy of the $Bi_2Te_{2.5}Se_{0.5}$ crystal structure, the transport properties of all samples were measured along the in-plane direction. The electrical conductivity and Seebeck coefficient of these specimens were measured from 300 to 500 K under a low-pressure He atmosphere using a standard four-probe method (ZEM-3, Ulvac-Riko). Polished samples with dimensions of approximately $\phi$ 6×1.5 mm were used to measuring thermal diffusivity $\lambda$ with a laser flash apparatus (LFA-467, Netzsch). The specific heat capacity $C_p$ was calculated using the Dulong-Petit law, which holds approximately within the measured temperature range. Bulk ensity $d$ was measured via the Archimedes method. The total thermal conductivity $\kappa$ was calculated according to $\kappa = \lambda C_p d$. A Hall measurement system (NYMS-I) was used to acquire the high-temperature Hall coefficient $R_H$ under an applied magnetic field of 1.5 T. The carrier concentration $n_H$ and Hall mobility $\mu_H$ were calculated from $n_H = 1/(R_H e)$ and $\mu_H = \sigma/ne$, respectively.

## 3. Results and discussion

### 3.1 Microstructure characterization

A series of sintered $x$ wt%$Ag_2Te/Bi_2Te_{2.5}Se_{0.5}$ composites ($x$ = 0, 0.2, 0.4, 0.6, 0.8, denoted as AT00,

Just Accepted

AT02, AT04, AT06, AT08, respectively) were used to analyze the effect of interfacial diffusion reactions on phase structure evolution. As displayed in Fig. 1a, the main Bragg diffraction peaks of all composites agree well with the standard $Bi_2Te_3$ PDF card (JCPDS 15-0863), confirming that $Bi_2Te_{2.5}Se_{0.5}$ constitutes the primary phase. A secondary $Ag_2Te$ phase, identifiable from the diffraction peak near 29°, appears in composites containing ≥0.6 wt% $Ag_2Te$, and its peak intensity increases obviously with rising $Ag_2Te$ content. To assess how interfacial diffusion reactions affect phase structure evolution, the patterns views in the 40°-43°range were examined in detail (Fig. 1b). Evidently, the principal diffraction peak shifts toward higher 2θ angles as the $Ag_2Te$ content increases. This contraction arises from the substitution of Bi atoms ($R_{Bi}$ = 1.55 Å) by smaller Ag atoms ($R_{Ag}$ = 1.45 Å) during interfacial reactions. Theoretical calculations predict lattice-parameter shrinkage along both crystallographic directions. Nevertheless, Rietveld-refined (Fig. S1) lattice parameters reveal anomalous expansion along the c-axis, which cannot be explained solely interpreted by the substitution of Ag atoms at Bi sites (Fig. 1c). The obtained reduction in a-axis lattice parameters is consistent with the substitution effect caused by smaller Ag replacing larger Bi atoms. Meanwhile, an anomalous expansion in the c-axis parameter is observed. XPS measurements show Ag 3d peaks at approximately 374 and 368 eV, consistent with $Ag^+$ chemical states, while the Bi 4f peaks shift toward higher and the Te 3d peaks toward lower binding energy, consistent with the electron-density redistribution expected for coexisting Ag substitution at Bi sites and Ag intercalation near Te (Fig. S2). In addition, formation energies for Ag occupying Bi sites, Ag residing in van der Waals gaps, and the $Ag_2Te$ phase are calculated via density functional theory (DFT)-based first-principles calculations, yielding values of -0.21 eV, -0.23 eV, and -0.06 eV, respectively (Table S3). The calculated results demonstrate that Ag preferentially occupies van der Waals gaps and subsequently substitutes at Bi sites when incorporated into $Bi_2Te_{2.5}Se_{0.5}$, and $Ag_2Te$ precipitates once the solubility limit is exceeded. Fig. 1d shows a schematic atomic model upon on Rietveld refinement and STEM results, illustrating Ag substitution on Bi sites and

Just Accepted

intercalation inside van der Waals gaps. Similar results were also observed in other $Bi_2Te_3$-based composites [31-33]. In particular, Te atoms with large atomic radius can also occupy the van der Waals gap [13], further supporting the existence of interstitial Ag atoms. This structural feature can weaken interlayer interactions, enhancing anharmonicity in the TE material and promoting the scattering of high-frequency phonons [34]. The above results indicate that the interfacial reaction causes part of Ag in $Ag_2Te$ to enter the Bi site and van der Waals gap, and the rest exists in the form of an $Ag_2Te$ second phase. This helps explain the influence of interfacial reactions on the electrical and thermal transport properties of $Bi_2Te_{2.5}Se_{0.5}$.

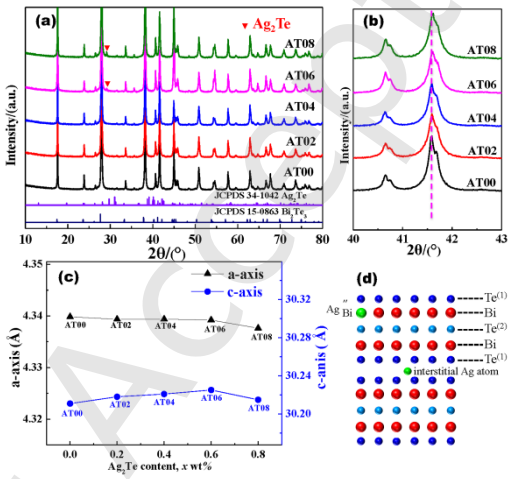



**Fig. 1 Phase structure evolution with $Ag_2Te$ addition.** (a) $Ag_2Te/Bi_2Te_{2.5}Se_{0.5}$ composites XRD patterns. (b) Close-up view of the diffraction peaks between 40°-43°. (c) Variation of lattice parameters with $Ag_2Te$ content. (d) Schematic atomic model depicting Ag substitution at Bi sites and van der Waals gap intercalation.

The backscattered electron image and corresponding elemental mapping images for composite AT06 are shown in Fig. 2. From the microstructure image, it was found that the composites consisted of gray and black contrast (Fig. 2a). Elemental mapping analysis was carried out to identify the chemical compositions of these two contrast regions. Bi, Te and Se elements are homogeneously distributed in gray areas (Fig. 2b, Fig. 2c and Fig. 2d), proving that this area is the $Bi_2Te_{2.5}Se_{0.5}$ matrix. However, Te and Ag accumulate

Just Accepted

specifically in black areas and coincide very well with each other, indicating that black contrast regions correspond to the $Ag_2Te$ phase. These observations confirm that the gray regions belong to $Bi_2Te_{2.5}Se_{0.5}$, whereas the darker regions correspond to the $Ag_2Te$ secondary phase, in good agreement with the XRD results. The secondary phase is important for optimizing electrical and thermal transport properties [25,26].

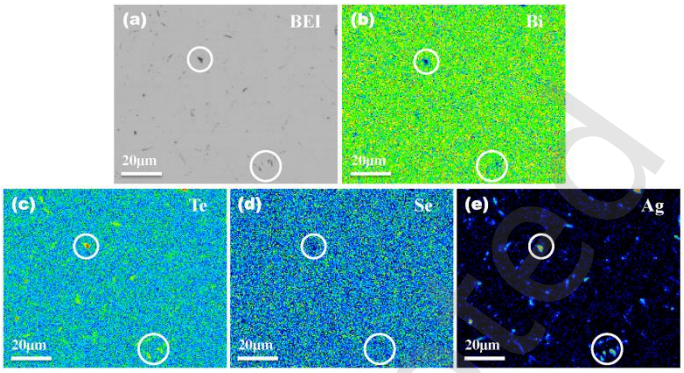



**Fig. 2 Microstructures and chemical compositions from EPMA.** (a) Backscattered electron image of AT06. (b)-(e) WDS elemental mapping of Bi, Te, Se and Ag, respectively

In order to verify the presence of $Ag_2Te$ in composites, the transmission electron microscopy (TEM) was performed to characterize the composition and atomic structure of $Ag_2Te/Bi_2Te_{2.5}Se_{0.5}$ composite. The HAADF micrograph reveals nanoscale pores distributed throughout the $Bi_2Te_{2.5}Se_{0.5}$ matrix (Fig. 3a). The X-ray energy dispersive spectroscopy (EDS) was used to analyze the chemical composition, as shown in Fig. 3b. It can be seen that the Ag is enriched at Bi and Se deficient position, and the Te in corresponding regions is not deficient, indicating that Ag and Te form compounds in these regions. These Ag-Te compounds vary in size from the nanometer scale to micrometer scale. However, Bi, Te and Se are uniformly distributed in other region, indicating the region is $Bi_2Te_{2.5}Se_{0.5}$ matrix. To examine the phase structure of Ag-Te compounds, the magnified HAADF-STEM image from Area 1 in Fig. 3a is shown in Fig. 3c. The crystal structure model of $Ag_2Te$ matches well with the atomic-scale HAADF-STEM image, where Ag and Te are represented by red spheres and green spheres, respectively. The fast Fourier transform (FFT) pattern (inset in Fig. 3c) matches the diffraction pattern of $Ag_2Te$ viewed along the [010]

Just Accepted

zone axis, which demonstrates that $Ag_2Te$ has room temperature Alpha phase structure. The EDS maps (Fig. 3d) from Fig. 3a are dominated by Te and Ag, whose distributions are very uniform, also identifying this region as $Ag_2Te$. A magnified HAADF-STEM image of $Bi_2Te_{2.5}Se_{0.5}$ in Area 2 is displayed in Fig. 3e. The typical quintuple layer of $Bi_2Te_{2.5}Se_{0.5}$ can be clearly seen. However, there is distortion between atomic layers, which may be caused by dislocations. To clearly show the dislocations, the inverse fast Fourier transform for HRTEM image was performed, as shown in Fig. 3f. Dislocations in the lattice are clearly visible, as marked by the red "⊥". On the other hand, some kinking exists in the $Bi_2Te_{2.5}Se_{0.5}$ matrix. Fig. 3g (elements line scan) shows that the Ag, Te, and Bi elemental contents exhibit opposite trends. The line scan passed through the $Ag_2Te$ and $Bi_2Te_{2.5}Se_{0.5}$ regions. In some areas with high Ag and Te content, the Bi content is almost zero, indicating that the area is the $Ag_2Te$ phase. Nevertheless, minor amounts of Ag are still detected within $Bi_2Te_{2.5}Se_{0.5}$ domains with high Bi and Te signals. This indicates that the interfacial diffusion takes place between the $Ag_2Te$ phase and the $Bi_2Te_{2.5}Se_{0.5}$ (the effective diffusion distance is approximately 165 nm). The diffused Ag may enter Bi sites or van der Waals gaps. Combined with results of XRD, it can be confirmed that Ag has entered the Bi positions and van der Waals gap. The interfacial diffusion reactions can modulate carrier concentration, thereby tuning electrical transport properties. Meanwhile, point defects originate from interfacial diffusion reactions, whereas dislocations and nanopores are generated jointly by sintering and interfacial reactions. These multiscale structural defects, together with dispersed $Ag_2Te$ secondary phase particles, strengthen phonon scattering and thus enable effective modulation of thermal transport properties. Notably, $Ag_2Te$ itself is a high-performance TE material, and its incorporation does not compromise the matrix quality, unlike conventional secondary phases that often degrade the $Bi_2Te_{2.5}Se_{0.5}$ matrix performance. Thus, integrating $Ag_2Te$ into $Bi_2Te_{2.5}Se_{0.5}$ presents a promising strategy for developing composites with superior TE properties. These multiscale microstructural features, including point defects, dislocations, nanopores and

Just Accepted

dispersed $Ag_2Te$ secondary phases, are expected to modify both carrier and phonon transport behaviors, as discussed in the following section.

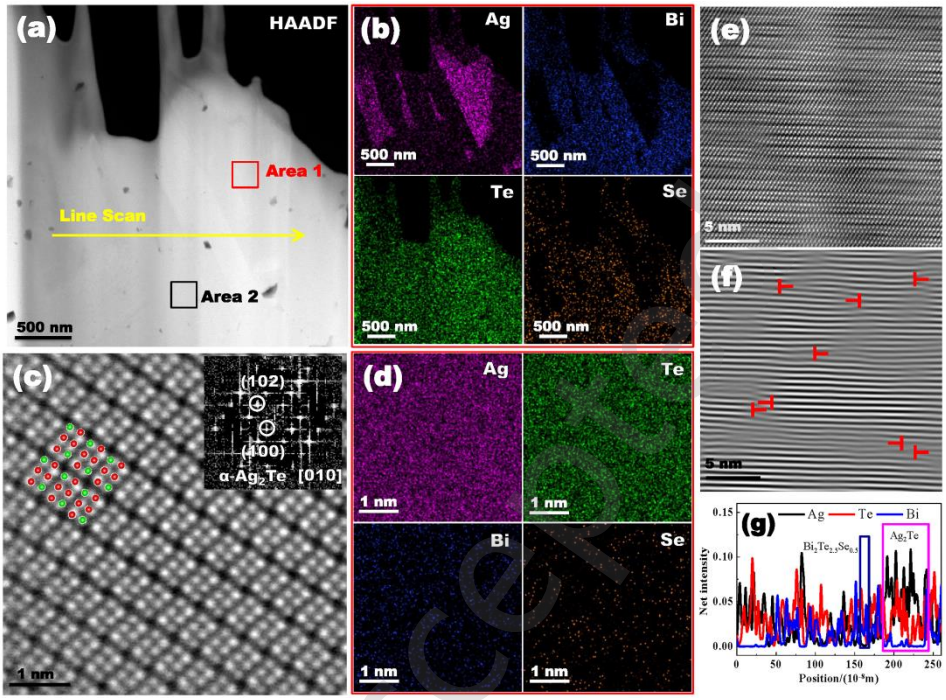



**Fig. 3 HAADF STEM and EDS analyses of the atomic structure.** (a) HAADF-STEM image of AT04. (b) Elemental mapping images of Ag, Bi, Te and Se of (a). (c) High-resolution HAADF-STEM images from the area 1 in (a), and the inset is the corresponding fast Fourier transform (FFT) image. (d) Elemental mapping images of Ag, Bi, Te and Se from (c). (e) High-resolution HAADF-STEM images from the area 2 in (a). (f) The inverse fast Fourier transform image of (e), clearly showing dislocations. (g) Elemental line scanning of Ag, Te and Bi of yellow line in (a).

### 3.2 Thermoelectric properties

To investigate the effects of $Ag_2Te$ on the electrical transport properties of $x$ wt%$Ag_2Te$/$Bi_2Te_{2.5}Se_{0.5}$ composites, the electrical conductivity ($\sigma$), carrier concentration ($n_H$) and Hall mobility ($\mu_H$) were measured at temperatures from 300 K to 500 K. For all samples, $\sigma$ decreases monotonically with rising temperature, which is characteristic of degenerate semiconducting or metallic-like conduction behavior (Fig. 4a).

Just Accepted

Compared with pristine $Bi_2Te_{2.5}Se_{0.5}$, the $Ag_2Te/Bi_2Te_{2.5}Se_{0.5}$ composites exhibit a monotonic decrease in $\sigma$ as $Ag_2Te$ content rises $Ag_2Te$ content. The $\sigma$ follows the relation $\sigma = n_H e \mu_H$, where $n_H$, e and $\mu_H$ are the carrier concentration, elementary charge, and carrier mobility, respectively. To elucidate the origin of the decrease in $\sigma$ with increasing $Ag_2Te$ content, both $n_H$ and $\mu_H$ were measured via the Hall effect, and the results are presented in Fig. 4b and Fig. 4c, respectively.

It is well known that ball milling refines particle sizes and greatly suppresses thermal conductivity. However, it also induces the donor-like effect, which drastically raises the $n_H$ of *n*-type $Bi_2Te_{2.5}Se_{0.5}$. This effect accounts for the poor TE performance observed, especially near room temperature. The $n_H$ is seen to decrease monotonically with increasing $Ag_2Te$ content (Fig. 4b) in this work. The decrease in $n_H$ arises from the suppression of donor-like effects and doping effects caused by interfacial diffusion reactions, both resulting from the introduction of $Ag_2Te$. Research [14,35] indicates that interstitial Ag raises the formation energy of $V_{Te}^{\cdot\cdot}$. Our calculation results indicate that both Ag at Bi sites and Ag in van der Waals gaps increase the vacancy formation energy $V_{Te}^{\cdot\cdot}$ (Table S4), thus inhibiting the formation of these vacancies in the $Bi_2Te_{2.5}Se_{0.5}$ matrix and curtailing electron production. This, in turn, suppresses the process shown in Eq. (1). In single crystal $Bi_2Te_{2.5}Se_{0.5}$, holes are the majority carriers, whereas in polycrystalline $Bi_2Te_{2.5}Se_{0.5}$, electrons dominate. This difference stems from the strong donor-like effect [36,37] created during powder metallurgy processes (Eq. (2)). By increasing the formation energy of $V_{Te}^{\cdot\cdot}$, interstitial Ag also mitigates the donor-like effect and further reduces the generation of electrons. Incorporation of an Ag atom into the $Bi_2Te_{2.5}Se_{0.5}$ lattice involves substitution of a Bi atom, generating an $Ag_{Bi}^{''}$ dopant and a $Bi_{Te}^{'}$ antisite defect. This process reduces the number of anion vacancies, thereby neutralizing more electrons (Eq. (3)). It is therefore believed that Ag at interstitial and Bi substitutional sites controls $n_H$ by increasing the vacancy formation energy and providing doping. This mechanism suppresses donor-like effects while forming antisite defects, including $Ag_{Bi}^{''}$ and $Bi_{Te}^{'}$. The defect

Just Accepted

chemical reactions describing the donor-like effect associated with Te vacancies and point defect evolution involving Ag are shown as follows.

$$Ag+V_{Te}^{\cdot\cdot}+2e' \rightarrow Ag_i^{\cdot}+e' \quad (1)$$

$$2V_{Bi}^{'''}+3V_{Te}^{\cdot\cdot}+Bi_{Te}^{'} \rightarrow V_{Bi}^{'''}+Bi_{Bi}^{\times}+4V_{Te}^{\cdot\cdot}+6e' \quad (2)$$

$$Ag+Bi_{Bi}^{\times}+V_{Te}^{\cdot\cdot}+6e' \rightarrow Ag_{Bi}^{''}+Bi_{Te}^{'}+e' \quad (3)$$

Below 420 K, the $\mu_H$ of all composites exceeds that of the matrix, with a slight enhancement at 300 K. Above 420 K, the enhancement diminishes or the composite mobility falls below that of the matrix (Fig. 4c). This change is due to the well-known phase transition of $Ag_2Te$, which occurs at around 420 K. The band gap of $Ag_2Te$ increases from 0.05 eV before the transition to 0.20 eV after it [38]. In contact with $Bi_2Te_{2.5}Se_{0.5}$ (band gap 0.18 eV [13]), semiconductor contact theory indicates the occurrence of energy band bending, interfacial charge transfer, and the establishment of a built-in electric field. Before the phase transition, the built-in electric field formed at the $Ag_2Te/Bi_2Te_{2.5}Se_{0.5}$ interface is directed from $Ag_2Te$ to $Bi_2Te_{2.5}Se_{0.5}$ (Fig. 4d). Electrons passing across the heterointerface are accelerated by this built-in electric field. In addition, $Ag_2Te$ exhibits high intrinsic $\mu_H$. Both effects jointly enhance the overall $\mu_H$. Although the substantial band gap difference between the two materials tends to hinder mobility, the final outcome is a net increase. After the phase transition, the direction of the built-in electric field reverses, now pointing from $Bi_2Te_{2.5}Se_{0.5}$ to $Ag_2Te$ (Fig. 4d). Electrons crossing the interface experience a decelerating force. At this point, the band gap difference between the two materials is small and exerts little influence on mobility. Meanwhile, the $\mu_H$ of post transition $Ag_2Te$ remains high, which benefits the composite. Nevertheless, the final $\mu_H$ remains nearly unchanged or even decreases. The temperature dependence of mobility reveals the dominant scattering mechanism. In the $\log(\mu_H)$ *versus* $\log(T)$ plot (the inset of Fig. 4c), $\mu_H$ exhibits a $T^{-1.5}$ dependence across the whole temperature range, consistent with acoustic phonon scattering as the main mechanism, which excludes the possibility that mobility variation arises from changes in defect scattering.

Just Accepted

From the above analysis, it is evident that the phase transition provides an additional interfacial modulation channel, rather than being the sole origin of the temperature dependence of $\mu_H$. It is worth noting that built-in electric field modulation does not alter the dominant acoustic phonon scattering mechanism. It only provides additional acceleration/deceleration effect for carriers, superimposed on phonon scattering. However, although $Ag^+$ ions become mobile above 420 K, their contribution to the Hall signal is expected to be negligible [39,40], so the mobility anomaly is more plausibly attributed to electronic band-structure reconstruction across the phase transition.

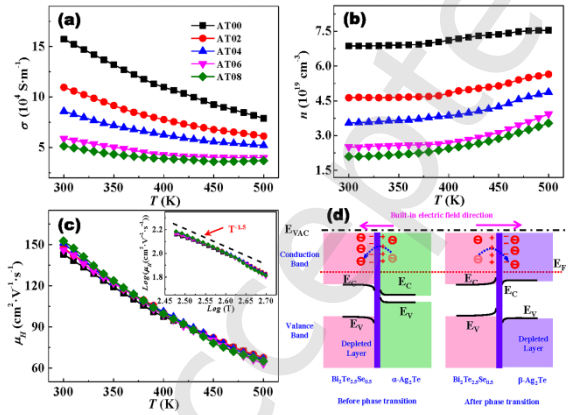



**Fig. 4 Electrical properties.** Temperature dependence of (a) electrical conductivity, (b) carrier concentration, (c) Hall mobility, of $x$ wt%$Ag_2Te/Bi_2Te_{2.5}Se_{0.5}$ ($x$ = 0, 0.2, 0.4, 0.6, 0.8). The inset in (c) is the log($\mu_H$) *versus* log($T$). (d) Schematic diagram of built-in electric field at heterogeneous interfaces.

The temperature dependent Seebeck coefficient ($\alpha$) is presented in Fig. 5a. Negative $\alpha$ is measured for both the matrix and the composites, which is characteristic of $n$-type conduction. This observation is further supported by the Hall coefficient data (Fig. 5b), confirming the dominant conduction type. With increasing $Ag_2Te$ content, $\alpha$ exhibits a gradual rise near room temperature, opposing the trends of $\sigma$ and $n_H$. For degenerate semiconductors, the $\alpha$ can also be described by the Mott formula (equation 4).

$$\alpha = \frac{8\pi^2 k_B^2 T m^*}{3eh^2}\left(\frac{\pi}{3n}\right)^{\frac{2}{3}} \quad (4)$$

The equation establishes a direct correlation between $\alpha$ and two key electronic parameters ($n_H$ and carrier effective mass $m$*). As mentioned above in Fig. 4b, $n_H$ decrease monotonically with increasing $Ag_2Te$

Just Accepted

content. To elucidate the mechanisms underlying the observed $\alpha$ variation, the room-temperature Pisarenko plots based on the single parabolic band (SPB) model were constructed (Fig. 5c). The room-temperature $m^*$ values were derived following the same procedure as detailed in our earlier report [41], and the obtained values are compiled in Table S1. Apparently, the $m^*$ of all composites quickly rises with increasing $Ag_2Te$ content, indicating that the effect of $Ag_2Te$ on the band structure is significant, which is favorable for achieving a high $\alpha$. Consequently, the observed enhancement in $\alpha$ can be ascribed to the combined influences of a rising $m^*$ and a declining $n_H$ within the system.

Assuming a constant $m^*$, the Pisarenko plot (Fig. 5c) visualizes the theoretical $\alpha$-$n_H$ relation derived from the SPB model using the room-temperature $m^*$ of the $Bi_2Te_{2.5}Se_{0.5}$ matrix. In the absence of additional electron scattering within the $Ag_2Te/Bi_2Te_{2.5}Se_{0.5}$ composites, experimental $\alpha$ values should closely follow this theoretical curve. Accordingly, downward deviation of data points indicates enhanced carrier scattering. Consequently, the observed increase in $\alpha$ can be attributed to both a reduction in $n_H$ and the additional scattering introduced by the $Ag_2Te$ phase. However, after the $Ag_2Te$ phase transformation, the theoretical $\alpha$-$n_H$ curve derived from the SPB model (with the $m^*$ of the $Bi_2Te_{2.5}Se_{0.5}$ matrix at 450 K) is presented as the Pisarenko plot in Fig. S3. Unlike the room-temperature case, the measured $\alpha$ data for the composites no longer uniformly fall below the reference line. Instead, some points shift above it. Such a deviation pattern points to a reduced carrier scattering intensity following the structural change, corroborating the previously noted decrease in band-gap difference. Thus, the post-transition state exhibits a notably weakened scattering influence on electron transport.

In contrast to $\sigma$, the $\alpha$ of all composites presents an ascending trend with increasing $Ag_2Te$ content in the range of 300-500 K, which can be mainly ascribed to the markedly reduced $n_H$. As temperature elevates, the matrix shows a steady increase in $\alpha$. In contrast, the composites experience a clear degradation in $\alpha$ after intrinsic excitation, attributable to the progressive activation of bipolar thermal excitation caused by a

Just Accepted

decrease in $n_H$ or a decrease in band gap ($E_g$). To identify the dominant contributing factor, we estimated $E_g$ following the method reported in our previous work [41] (Table S1). The composites exhibit a marginal increase in $E_g$ for the composites relative to the pristine matrix, ruling out $E_g$ reduction as a major cause. Consequently, the downward shift of the $\alpha$-peak temperature with increasing $Ag_2Te$ content is primarily governed by the diminished $n_H$, which promotes earlier bipolar activation.

The power factor ($\alpha^2\sigma$) exhibits a non-monotonic dependence on $Ag_2Te$ loading. The AT04 sample attains a peak $\alpha^2\sigma$ of 3.10 $mW \cdot m^{-1} \cdot K^{-2}$ at room temperature, but this value decreases steadily as the test temperature further increases. In addition, cycling tests were performed (Fig. S4), and the results showed that both the $\sigma$ and the $\alpha$ exhibited good repeatability within five cycles, demonstrating the stability of the composite at high temperatures. For compositions exceeding AT04, the benefit derived from the enhanced $\alpha$ is outweighed by a more severe drop in $\sigma$, ultimately suppressing the overall $\alpha^2\sigma$. This suppression is largely due to the strong reduction in $\sigma$ induced by the $Ag_2Te$ phase. To achieve higher $\alpha^2\sigma$ in future work, a better trade-off between $\sigma$ and $\alpha$ could be pursued through compositional tuning or process optimization.

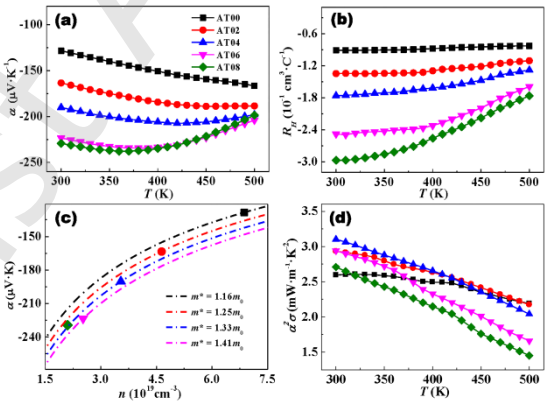



**Fig. 5 Electrical properties.** Temperature dependence of (a) Seebeck coefficient, (b) Hall coefficient, (d) power factor of $x$ wt%$Ag_2Te$/$Bi_2Te_{2.5}Se_{0.5}$ ($x$ = 0, 0.2, 0.4, 0.6, 0.8). (c) The Seebeck coefficient versus carrier concentration for the matrix at 300 K obtained by the Pisarenko relation.

By triggering concurrent changes in composition and microstructure, the $Ag_2Te$ incorporation synergistically boosts electrical transport and reduces thermal conductivity within the $Bi_2Te_{2.5}Se_{0.5}$ matrix.

Just Accepted

The addition of $Ag_2Te$ leads to a pronounced reduction in total thermal conductivity $\kappa$, as depicted in Fig. 6a, with the effect being most conspicuous at low temperatures. Quantitatively, $\kappa$ at 300 K decreases monotonically from 1.42 to 0.85 $W \cdot m^{-1} \cdot K^{-1}$ with increasing $Ag_2Te$ content, corresponding to a 40% reduction. The substantial reduction in $\kappa$, induced by the second-phase modification of both carrier and phonon transport, inevitably modifies the overall thermal transport behavior. $\kappa$ is generally decomposed into carrier thermal conductivity $\kappa_E$ and lattice thermal conductivity $\kappa_L$ parts. The carrier contribution was calculated using the Weidemann-Franz law relation $\kappa_E = L\sigma T$, with the Lorenz parameter $L$ determined from the SPB model under the assumption of dominant acoustic-phonon scattering ($r$ = -1/2), based on Fermi-Dirac statistics. $L$ is plotted in Fig. 6b and exhibit a temperature dependence consistent with that of the Seebeck coefficient. As shown in Fig. 5c, $Ag_2Te$ addition reduces the carrier concentration and the $\kappa_E$ gradually decreases with increasing $Ag_2Te$ content (Fig. 6c), a trend that closely mirrors the reduction in electrical conductivity.

$\kappa_L$ was calculated according to $\kappa_L = \kappa - \kappa_E$ and the results are shown in Fig. 6d. At 300 K, $\kappa_L$ first decreases with $Ag_2Te$ loading owing to defect and interface phonon scattering. It then rises at higher $Ag_2Te$ fractions. This trend originates from reduced $n_H$, which weakens carrier-phonon interaction. The temperature dependence of $\kappa_L$ first declines to a minimum and then undergoes an upturn, a feature largely governed by the bipolar contribution. $\kappa_L$ first declines with increasing temperature owing to stronger phonon-phonon scattering, reaches a minimum, and subsequently increases, implying that bipolar thermal diffusion takes over in this range. The calculated $\kappa_{L,\,min}$ for $Bi_2Te_{2.5}Se_{0.5}$ is 0.298 $W \cdot m^{-1} \cdot K^{-1}$ (Detailed information is provided in Section 9 of the Supporting Information). Our experimental minimum lattice thermal conductivity (about 0.44 $W \cdot m^{-1} \cdot K^{-1}$) is still higher than theoretical limit, indicating further space for phonon engineering. As the $Ag_2Te$ fraction increases, the threshold temperature for bipolar transport shifts to lower temperatures, leading to a stronger bipolar effect. The $T^{-1}$ relationship was adopted to assess

Just Accepted

how $\kappa_L$ changes with temperature in the regime dominated by Umklapp phonon scattering (Fig. S5). The results show that the $Bi_2Te_{2.5}Se_{0.5}$ material has obvious intrinsic excitation. The reduction in $n_H$ rather than the slight change in $E_g$ intensifies intrinsic excitation and accelerates the onset of bipolar diffusion. $E_g$ were estimated from Table S1 to clarify the key factor. The composites show only a marginal $E_g$ elevation over the pristine matrix, thereby excluding $E_g$ reduction as a primary cause. As a result, the shift of the intrinsic excitation temperature to lower values with increasing $Ag_2Te$ content is largely ascribable to the decrease in $n_H$.

The material quality factor $\beta$, calculated at room temperature via equation 5, is adopted to evaluate the comprehensive carrier-phonon transport performance.

$$\beta = 5.745 \times 10^{-6} \frac{\mu_H}{\kappa_L} \left(\frac{m^*}{m_0}\right)^{\frac{3}{2}} T^{5/2} \quad (5)$$

As listed in Table S1, $\beta$ initially increases with $Ag_2Te$ content, reaches a maximum, and then declines. Compared with the pristine $Bi_2Te_{2.5}Se_{0.5}$ matrix, the composites exhibit superior $\beta$ values despite a non-monotonic decrease in $\kappa_L$, primarily owing to the combined enhancement of $\mu_H$ and $m^*$. Notably, the AT04 sample achieves the highest $\beta$ among all compositions, benefiting from the concurrent rise in $\mu_H$ and $m^*$ alongside a small change in $\kappa_L$, resulting in a 42% improvement over the pristine matrix at room temperature. The $\beta$ at 450 K was calculated to probe the effect of the phase transition. With increasing $Ag_2Te$ loading, the calculated $\beta$ values show a marginal increase at low fractions, followed by a decrease at higher fractions, suggesting a composition-dependent modulation (Table S2). Since a large quality factor $\beta$ generally correlates with a high $ZT$, the observed enhancement validates the effectiveness of this $\beta$-oriented strategy for improving TE performance. Furthermore, it highlights the composition-dependent modulation triggered by the $Ag_2Te$ phase transition.

Just Accepted

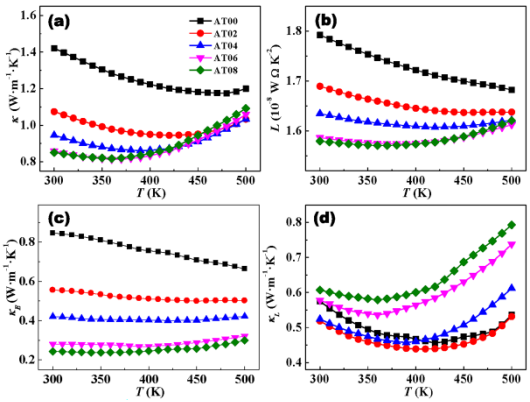



**Fig. 6 Thermal properties.** Temperature dependence of (a) total thermal conductivity, (b) Lorentz number, (c) carrier thermal conductivity, (d) lattice thermal conductivity of $x$ wt%$Ag_2Te$/$Bi_2Te_{2.5}Se_{0.5}$ ($x$ = 0, 0.2, 0.4, 0.6, 0.8).

The temperature-dependent dimensionless figure of merit ($ZT$) for all samples is presented in Fig. 7a. In the room-temperature region, the $Ag_2Te$/$Bi_2Te_{2.5}Se_{0.5}$ composites exhibit substantially higher $ZT$ than the pristine $Bi_2Te_{2.5}Se_{0.5}$ matrix, owing to the combined benefits of enhanced $\alpha^2\sigma$ and reduced $\kappa$. With increasing $Ag_2Te$ content, $ZT$ first increases and then decreases, with the AT04 sample reaching a peak of ~1.23 at 410 K. Notably, the $ZT$ maximum progressively shifts to lower temperatures with increasing $Ag_2Te$ fraction, highlighting the capability of $Ag_2Te$ for tuning the near-room-temperature TE performance of $Bi_2Te_{2.5}Se_{0.5}$-based materials. The AT04 sample delivers the highest room-temperature $ZT$ of 0.98, marking an 80% improvement over the unmodified matrix. As depicted in Fig. 7b, the $ZT$ values obtained within 300-500 K are competitive against most previously reported results for similar working temperature ranges. Compared with previously reported $Ag_2Te$/$Bi_2Te_{2.5}Se_{0.5}$ composites [30], our AT04 sample achieves competitive $ZT$, which originates from well-regulated carrier concentration, phase-tunable interfacial built-in electric field, and the intrinsically excellent TE properties of $Ag_2Te$ (Fig. S6). The maximum $ZT$ value exceeds other reported data (Fig. S7). To assess the practical service temperature window, we calculated the average $ZT$ ($ZT_{ave}$) over two ranges (300-400 K and 300-500 K), as shown in Fig. 7c. The AT04 sample achieves a $ZT_{ave}$ exceeding 1.13 across both ranges, substantially outperforming

Just Accepted

the matrix and outperforming the matrix and suggesting reliable performance from 300 to 500 K. Furthermore, the $ZT_{ave}$ of the AT04 composite is considerably higher than reported literature values (Fig. S8). Notably, the AT04 sample yields a maximum efficiency of ~8.9% at $\Delta T$ = 200 K (Fig. 7d). The theoretical conversion efficiency was calculated under cold-side temperature $\Delta T$ = 300 K. Collectively, these results confirm that $Ag_2Te$ incorporation effectively optimizes the TE properties of $Bi_2Te_{2.5}Se_{0.5}$, particularly in the near-room-temperature regime.

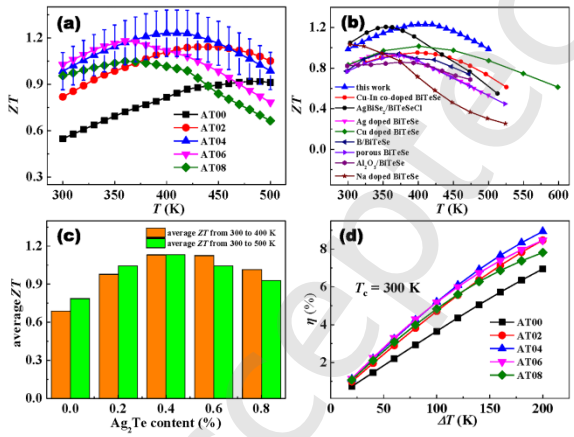



**Fig. 7 *ZT* values and conversion efficiency.** (a) Temperature dependence of *ZT* values of *x* wt%$Ag_2Te/Bi_2Te_{2.5}Se_{0.5}$ (*x* = 0, 0.2, 0.4, 0.6, 0.8). (b) comparison of *ZT* (AT04) in this work with other reported $Bi_2Te_3$-based composite systems. (c) $ZT_{ave}$ for all samples at different temperature ranges. (d) calculated conversion efficiency $\eta$ of $Ag_2Te/Bi_2Te_{2.5}Se_{0.5}$ composite.

## 4. Conclusions

A series of *n*-type $Ag_2Te/Bi_2Te_{2.5}Se_{0.5}$ composites were fabricated via mechanical alloying combined with spark plasma sintering. Owing to interfacial diffusion between superionic $Ag_2Te$ and $Bi_2Te_{2.5}Se_{0.5}$ matrix, partial Ag from $Ag_2Te$ diffuses into the $Bi_2Te_{2.5}Se_{0.5}$ lattice to substitute for Bi atoms or intercalate into van der Waals gaps, while the residual $Ag_2Te$ forms a secondary phase. The diffused Ag suppresses the detrimental donor-like effect and decreases carrier concentration. Below 420 K, the built-in electric field at hetero-interfaces enhances carrier mobility. Multiscale defects and secondary-phase particles

Just Accepted

jointly reduce lattice thermal conductivity. The AT04 composite achieves optimal TE performance with a peak *ZT* ~1.23 at 410 K and room-temperature *ZT* of 0.98. This work offers a feasible route to synergistically tune carrier-phonon transport for high-performance *n*-type $Bi_2Te_{2.5}Se_{0.5}$.

**Acknowledgments**

This work was supported by the National Natural Science Foundation of China (No. 52361038, 52502248), Jiangxi Provincial Natural Science Foundation (No. 20232BAB204023, 20252BAC240399), the Natural Science Foundation of Jiujiang city (No. 2025_000772, 2025_001264), the Science and Technology Research Project of Jiangxi Provincial Department of Education (No. GJJ2501821, GJJ2401817), the Natural Science Foundation of Shandong Province (No. ZR2024QE089), the China Postdoctoral Science Foundation (No. 2024M753321). Theoretical calculations were performed at the Institute for Genetic Engineering of Materials, Henan Academy of Sciences. The authors thank Xianfeng Ye (Henan Academy of Sciences) for his assistance with the theoretical calculations.

**Author contributions**

Shifang Ma: writing - original draft, writing - review & editing, funding acquisition, methodology. Daming Du: investigation. Ming Lin: methodology. Jinzhao Guan: investigation. Shaoqiu Ke: methodology. Cuncheng Li: methodology. Jian Yu: writing - review & editing. Zhiyuan Liu: writing - review & editing.

**Availability of data and materials**

The data that support the findings of this study are available from the corresponding author upon reasonable request.

**Competing interests**

Just Accepted

The authors have no competing interests to declare that are relevant to the content of this article.

## References


[1] Mao J, Zhu HT, Ding ZW*, et al.* High thermoelectric cooling performance of n-type $Mg_3Bi_2$-based materials. *Science* 2019, **365**: 495-498.

[2] Ke SQ, Liang D, Nie XL*, et al.* Multi-beam spark plasma sintering and excellent performance of $Bi_{0.5}Sb_{1.5}Te_3$/epoxy thermoelectric films with insulating substrates. *Energy Environ Sci* 2023, **16**: 5434-5443.

[3] Duan XK, Hu QX, Jiang YZ*, et al.* Cold spraying-an effective shapable method for preparing high-performance $Bi_2Te_3$-based thermoelectrics. *J Mater Sci Technol* 2026, **270**: 305-312.

[4] Wu ZH, Sun X, Luo D*, et al.* Optimizing the thermal and energy efficiency of a thermoelectric-based battery thermal management system via adaptive control strategies and phase change materials. *Energy* 2026, **344**: 139845.

[5] Lin SQ, Guo LL, Wang XH*, et al.* Revealing the promising near-room-temperature thermoelectric performance in $Ag_2Se$ single crystals. *J Materiomics* 2023, **9**: 754-761.

[6] Yang DW, Xing YB, Wang J*, et al.* Multifactor roadmap for designing low-power-consumed micro thermoelectric thermostats in a closed-loop integrated 5G optical module. *Interdiscip Mater* 2024, **3**: 326-337.

[7] Xie HY, Zhao LD, Kanatzidis MG. Lattice dynamics and thermoelectric properties of diamondoid materials. *Interdiscip Mater* 2024, **3**: 5-28.

[8] Wang LS, Xu SJ, Yang J*, et al.* Achieving ultrahigh power factor in $Mg_3(Sb,Bi)_2$-based thermoelectric alloys sintered by introducing elemental Mg and W. *J Adv Ceram* 2025, **14**: 9221029.


Just Accepted

[9] Zhu J, Wang Y, Liu H*, et al.* Carbon fiber/thermoelectric $Ag_2S$ core-shell structure-based temperature-pressure dual-mode sensors. *J Adv Ceram* 2025, **14**: 9221073.

[10] Li ZL, Yang XQ, Gao Z*, et al.* Remarkable average thermoelectric performance of the highly oriented Bi(Te,Se)-based thin films and devices. *J Materiomics* 2024, **10**: 366-376.

[11] Zhu H, Deng ZM, Qu YH*, et al.* Strong texture in nanostructured bulk $Bi_{0.5}Sb_{1.5}Te_3$ leads to superior thermoelectric and mechanical performance. *J Mater Sci Technol* 2025, **232**: 267-275.

[12] Cho H, Back SY, Yun JH*, et al.* Thermoelectric properties and low-energy carrier filtering by Mo microparticle dispersion in an n-type $(CuI)_{0.003}Bi_2(Te,Se)_3$ bulk matrix. *ACS Appl Mater Interfaces* 2020, **12**: 38076-38084.

[13] Zhu B, Wan W, Cui J*, et al.* Point defect engineering: Co-doping synergy realizing superior performance in n-type $Bi_2Te_3$ thermoelectric materials. *Small* 2021, **17**: e2101328.

[14] Li L, Wei P, Yang MJ*, et al.* Strengthened interlayer interaction and improved room-temperature thermoelectric performance of Ag-doped n-type $Bi_2Te_{2.7}Se_{0.3}$. *Sci China Mater* 2023, **66**: 3651-3658.

[15] Lou LY, Yang JM, Zhu YK*, et al.* Tunable electrical conductivity and simultaneously enhanced thermoelectric and mechanical properties in n-type $Bi_2Te_3$. *Adv Sci* 2022, **9**: 2203250.

[16] Xie WJ, Tang XF, Yan YG*, et al.* Unique nanostructures and enhanced thermoelectric performance of melt-spun BiSbTe alloys. *Appl Phys Lett* 2009, **94**: 102111.

[17] Deng RG, Su XL, Hao SQ*, et al.* High thermoelectric performance in $Bi_{0.46}Sb_{1.54}Te_3$ nanostructured with ZnTe. *Energy Environ Sci* 2018, **11**: 1520-1535.

[18] Cai B, Zhuang HL, Pei J*, et al.* Spark plasma sintered Bi-Sb-Te alloys derived from ingot scrap: Maximizing thermoelectric performance by tailoring their composition and optimizing sintering time. *Nano Energy* 2021, **85**: 106040.

[19] Yang GS, Sang LN, Yun FF*, et al.* Significant enhancement of thermoelectric figure of merit in

Just Accepted

BiSbTe-based composites by incorporating carbon microfiber. *Adv Funct Mater* 2021, **31**: 2008851.

[20] Poudel B, Hao Q, Ma Y*, et al.* High-thermoelectric performance of nanostructured bismuth antimony telluride bulk alloys. *Science* 2008, **320**: 634-638.

[21] Liu Y, Zhang Y, Lim KH*, et al.* High thermoelectric performance in crystallographically textured n-type $Bi_2Te_{3-x}Se_x$ produced from asymmetric colloidal nanocrystals. *ACS Nano* 2018, **12**: 7174-7184.

[22] Liu Y, Zhang Y, Ortega S*, et al.* Crystallographically textured nanomaterials produced from the liquid phase sintering of $Bi_xSb_{2-x}Te_3$ nanocrystal building blocks. *Nano Lett* 2018, **18**: 2557-2563.

[23] Zhang WJ, Al-Maythalony BA, Gao FX*, et al.* Thermally stable inorganic $Bi_{0.4}Sb_{1.6}Te_3$/metal-organic framework (MOF) composites with 1-by-1 nm pore engineering towards mid-temperature thermoelectrics. *Energy Environ Sci* 2024, **17**: 5679-5690.

[24] Li JH, Tan Q, Li JF*, et al.* BiSbTe-based nanocomposites with high ZT: The effect of SiC nanodispersion on thermoelectric properties. *Adv Funct Mater* 2013, **23**: 4317-4323.

[25] Hu QJ, Guo JB, Zuo HY*, et al.* Enhanced thermoelectric properties of n-type $Bi_2Te_{2.7}Se_{0.3}$ materials by $TiO_2$ ceramic nanoparticle dispersion-induced energy filtering effect. *Ceram Int* 2023, **49**: 32144-32152.

[26] Zhang CH, Geng XJ, Chen B*, et al.* Boron-mediated grain boundary engineering enables simultaneous improvement of thermoelectric and mechanical properties in n-type $Bi_2Te_3$. *Small* 2021, **17**: 2104067.

[27] Haruna AY, Luo YB, Ma Z*, et al.* High thermoelectric performance in Cu-doped $Bi_2Te_{2.7}Se_{0.33}$ due to Cl doping and multiscale $AgBiSe_2$. *ACS Appl Mater Interfaces* 2023, **15**: 49259-49269.

[28] Chen T, Qin XY, Ming HW*, et al.* Enhancing thermoelectric performance of n-type $Bi_2Te_{2.7}Se_{0.3}$ through the incorporation of $MnSb_2Se_4$ nanoinclusions. *Chem Eng J* 2023, **467**: 143397.

[29] Tong YF, Huang WJ, Tan XJ*, et al.* Enhanced thermoelectric properties of p-type $Bi_{0.5}Sb_{1.5}Te_3$-$Cu_8GeSe_6$ composite materials. *ACS Appl Mater Interfaces* 2022, **14**: 55780-55786.

[30] Li SJ, Chen T, Yang SH*, et al.* Attaining high figure of merit in the n-Type $Bi_2Te_{2.7}Se_{0.3}$-$Ag_2Te$

Just Accepted

composite system via comprehensive regulation of its thermoelectric properties. *ACS Appl Mater Interfaces* 2023, **15**: 36457-36467.

[31] Zhu H, Deng ZM, Qu YH*, et al.* Cu-In co-doping and layered directional sintering for high thermoelectric efficiency and mechanical strength in $Bi_2(Te,Se)_3$. *Adv Funct Mater* 2025, **35**: 2422007.

[32] Li YC, Bai SL, Wen Y*, et al.* Realizing high-efficiency thermoelectric module by suppressing donor-like effect and improving preferred orientation in n-type $Bi_2(Te,Se)_3$. *Sci Bull* 2024, **69**: 1728-1737.

[33] Li HT, Chen LD, Guo Z*, et al.* Ultra-low lattice thermal conductivity realizing ultra-high performance $Bi_{0.48}Sb_{1.52}Te_3$-based thermoelectric material and module. *Energy Environ Sci* 2024, **17**: 6091-6101.

[34] Chen ZW, Zhang XY, Pei YZ. Manipulation of phonon transport in thermoelectrics. *Adv Mater* 2018, **30**: 1705617.

[35] Lu MP, Liao CN, Huang JY*, et al.* Thermoelectric properties of Ag-doped $Bi_2(Se,Te)_3$ compounds: dual electronic nature of Ag-related lattice defects. *Inorg Chem* 2015, **54**: 7438-7444.

[36] Hu LP, Zhu TJ, Liu XH*, et al.* Point defect engineering of high-performance Bismuth-Telluride-Based thermoelectric materials. *Adv Funct Mater* 2014, **24**: 5211-5218.

[37] Hu LP, Wu HJ, Zhu TJ*, et al.* Tuning multiscale microstructures to enhance thermoelectric performance of n-type Bismuth-Telluride-Based solid solutions. *Adv Energy Mater* 2015, **5**: 1500411.

[38] Pei YZ, Heinz NA, Snyder GJ. Alloying to increase the band gap for improving thermoelectric properties of $Ag_2Te$. *J Mater Chem* 2011, **21**: 18256.

[39] Jung DY, Kurosaki K, Ohishi Y*, et al.* Effect of phase transition on the thermoelectric properties of $Ag_2Te$. *Mater Trans* 2012, **53**: 1216-1219.

[40] Stuhrmann CHJ, Kreiterling H, Funke K. Ionic Hall effect measured in rubidium silver iodide. *Phys Chem Chem Phys* 2001, **3**: 2557-2558.

[41] Ma SF, Zeng LJ, Du DM*, et al.* Grain boundary engineering simultaneously optimized thermoelectric

Just Accepted

and mechanical properties of BiSbTe alloys. *J Power Sources* 2024, **618**: 235191.

Just Accepted